Electronic Supplementary Material (ESI) for Journal of Materials Chemistry A.
This journal is © The Royal Society of Chemistry 2022

Electronic Supplementary Information for

Synergistically coupling Pt with Ni toward accelerated water dissociation for enhanced alkaline hydrogen evolution†

Jiangnan Guo,‡ Jinlong Liu,‡*, Xinxin Zhang, Xiyuan Guan, Muhong Zeng, Jiarong Shen, Jianing Zou, Qiuzhu Chen, Tian Wang, and Dong Qian*

College of Chemistry and Chemical Engineering, Central South University, Changsha 410083, China

‡ These authors contributed equally to this work.

* Corresponding authors. *E-mail addresses:* liujinlong@csu.edu.cn (J. Liu), qiandong6@vip.sina.com (D. Qian).

1. Experimental Section

1.1 Syntheses of Materials

Hydrochloric acid (HCl, 37%), ethanol, potassium hydroxide (KOH), aniline (99.5%), nickel(II) nitrate hexahydrate ($NiCl_2 \cdot 6H_2O$, 99.995%), chloroplatinic acid hexahydrate ($H_2PtCl_6 \cdot 6H_2O$, Pt ≥37.5%), and ammonium persulfate (APS, $(NH_4)_2S_2O_8$, 99.99%) were purchased from Aladdin. While Pt/C (20 wt% of Pt on Vulcan XC72) and Nafion (5 wt%) were obtained from the Fuel Cell Store. All the chemical reagents used in this work were analytical grade, and they were utilized directly without any purification. In a typical synthesis procedure of PtNi-NC-900, 9 mL of concentrated hydrochloric acid was added to 14 mL of deionized water, which was stirred to cool down naturally to room temperature. Afterwards, 2 mL of aniline was added dropwise into the diluted hydrochloric acid solution to obtain mix solution A. Then, 2.5 g of APS was dissolved into 10 mL of deionized water, resulting in solution B. Both the solutions were cooled to 4 ℃ in a refrigerator. Next, the solutions A and B were mixed and maintained at 4 ℃ for 12 h, which undertook polymerization to form polyaniline. The obtained product was washed with deionized water to pH ≈ 7 and collected by vacuum filtration. 0.3 mmol $NiCl_2 \cdot 6H_2O$ and 0.2 mmol $H_2PtCl_6 \cdot 6H_2O$ were dissolved in 20 mL of deionized water under magnetic agitation for 15 min, and then the collected polyaniline was dispersed in the above solution by stirring for another 1 h. After aging for 2 h, the solution was frozen using liquid nitrogen, then dried by lyophilization. The collected solid was transferred into a porcelain boat and heated (5 $^oC\ min^{-1}$) to 900 ^oC under a N_2 flow in a tube furnace, then annealed at 900 ^oC for 2 h, thereby giving the final product of PtNi-NC-900. For comparison, PtNi-NC-800 and PtNi-NC-1000 were also prepared by the similar procedures through controlling the pyrolysis temperatures at 800 and 1000 ^oC, respectively. Meanwhile, Pt-NC-900 was synthesized by the same method with the absence of $NiCl_2 \cdot 6H_2O$, and NC-900 was prepared by direct pyrolysis of polyaniline at 900 ^oC for 2 h in N_2 atmosphere.

1.2 Materials Characterizations

Scanning electron microscopy (SEM) images were taken on a Zeiss Sigma 300 filed-scanning electron microscope (FE-SEM). Transmission electron microscope (TEM) images, high-resolution TEM (HRTEM) images, selected area electron diffraction (SAED), and elemental mappings were obtained on a Tecnai G2 60-300 HOLO transmission electron microscope (TEM) with an image corrector and an energy-dispersive X-ray spectroscopy detector. X-ray diffraction (XRD) patterns were collected on a X'Pert PRO MPD X-ray diffractometer with Cu Kα radiation. N_2 adsorption-desorption isotherms were recorded on a Tristar 3000 surface area and pore analyzer. X-ray

photoelectron spectroscopy (XPS) data were obtained on a Thermo Scientific K-Alpha X-ray photoelectron spectrometer equipped with a monochromatic Al Kα source.

1.3 Electrochemical Measurements

The electrochemical properties of obtained powdery catalysts were investigated in a standard three-electrode system by the rotating disk electrode (RDE) method on a CHI 760E electrochemical workstation. Firstly, the as-prepared sample was dispersed in a mixed solution consisting of deionized water, ethanol, and 5 wt% Nafion by a volume ratio of 10:9:1 under sonication for 1 h. 10 μL of the catalyst ink (4.0 mg mL^{-1}) was then transferred onto a glassy carbon RDE (diameter = 5 mm, Pine Research Instrumentation), which was dried naturally in the air to serve as the working electrode. A carbon rod, a Hg/HgO electrode, and 1.0 M KOH aqueous solution were employed as the counter electrode, reference electrode, and electrolyte, respectively. During the electrochemical testing, the working electrode was rotated at 1600 rpm and a flow of N_2 was maintained to remove H_2 bubbles formed on the RDE surface. All potentials were referenced to a reversible hydrogen electrode by adding a value of (0.098 + 0.0592×pH), and all polarization curves were calibrated by considering the *iR* contribution within the cell.

1.4 Computation Methods

The spin-polarized density functional theory (DFT) calculations were carried out using the Vienna Ab initio Simulation Package (VASP) software.[1, 2] To be specific, $PtNi_3$(111) and Pt(111) slab models were built based on the HRTEM results and element content analysis, representing the catalytic surfaces of PtNi-NC-900 and commercial Pt/C catalysts, respectively. According to the experimentally observed Tafel slope values of PtNi-NC-900 and 20% Pt/C, it can be inferred that the alkaline HER processes on $PtNi_3$(111) and Pt(111) surfaces are much more likely to follow the Volmer-Heyrovsky mechanism that generally involves four steps, namely, the adsorption of water molecule on the active site to form $*H_2O$, the dissociation of $*H_2O$ to generate *H and *OH, the subsequent desorption of *OH, and the final desorption of *H to release gaseous H_2.[3, 4] All computations were performed using the projected augmented wave (PAW) method and Perdew-Burke-Ernzerhof (PBE) exchange-correction functional to describe the core electrons and the electron interactions, respectively, under the generalized gradient approximation (GGA) with a plane-wave cut-off energy of 600 eV.[5-7] Dispersion correction was also considered in Grimme's scheme using DFT-D3 method.[8] For the geometry optimization, the top two layers of atoms were relaxed completely, whilst the bottom two layers of atoms were fixed. A Γ-point-centered

Monkhorst-Pack k-point grid of 4×4×1 was adopted to sample the Brillouin zone. The energy and force convergence thresholds were set to be 1×10^{-5} eV and 0.02 eV $Å^{-1}$, respectively. For the calculations of density of states, the k-point grid was increased to 12×12×1. A vacuum space of 15 Å was created in the *c* direction to avoid interactions between mirror images.

Under alkaline conditions (e.g., 1.0 M KOH, pH = 14), the HER via the Volmer-Heyrovsky mechanism involves the following steps:[3, 4]

$$* + H_2O \rightarrow *H_2O \quad (1)$$

$$*H_2O \rightarrow *H + *OH \quad (2)$$

$$*H + *OH + e^- \rightarrow *H + OH^- \quad (3)$$

$$*H \rightarrow * + 1/2\ H_2 \quad (4)$$

To calculate the free energy diagrams, the concept of computational hydrogen electrode proposed by Nørskov et al. was adopted, that is, the chemical potential of the ($H^+ + e^-$) couple equals to 1/2 H_2 at pH = 0 in the electrolyte and 1 bar of H_2 in the gas at 298.15 K.[9] Therefore, the reaction free energy of each elementary step above can be calculated by the following equation:

$$\Delta G = \Delta E + \Delta ZPE - T\Delta S + \Delta G_{pH} \quad (5)$$

where ΔE is the electronic energy difference directly available from the DFT computation, ΔZPE is the correction in zero-point energies (*ZPE*), T is the room temperature (here T = 298.15 K), ΔS is the entropy change, ΔG_{pH} is the correction for the H^+ free energy associated with the pH value (i.e., $\Delta G_{pH} = k_B T \times \ln10 \times pH$, k_B is the Boltzmann constant). Both ΔZPE and ΔS can be obtained from the vibration frequency analysis of the adsorbed species.

2. Supplementary Results

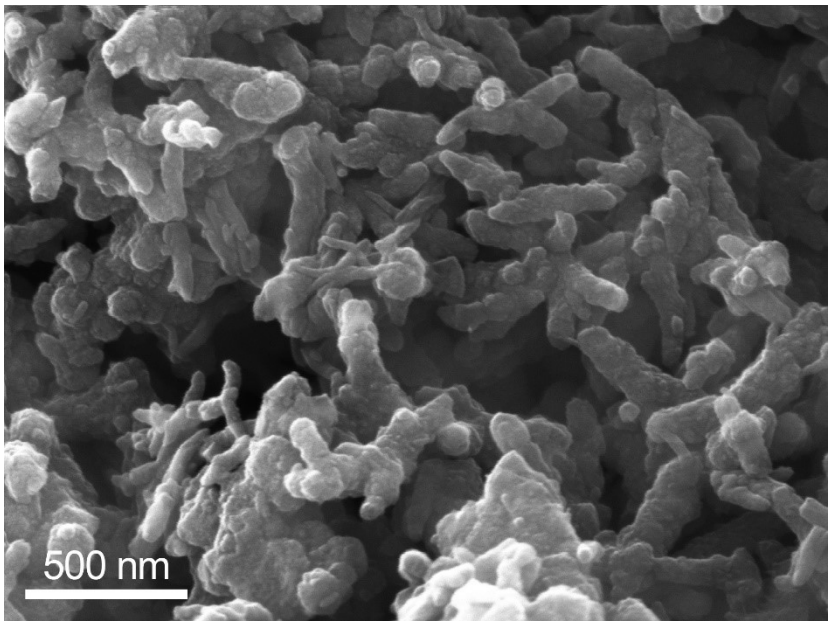

Fig. S1 Representative SEM image of polyaniline.

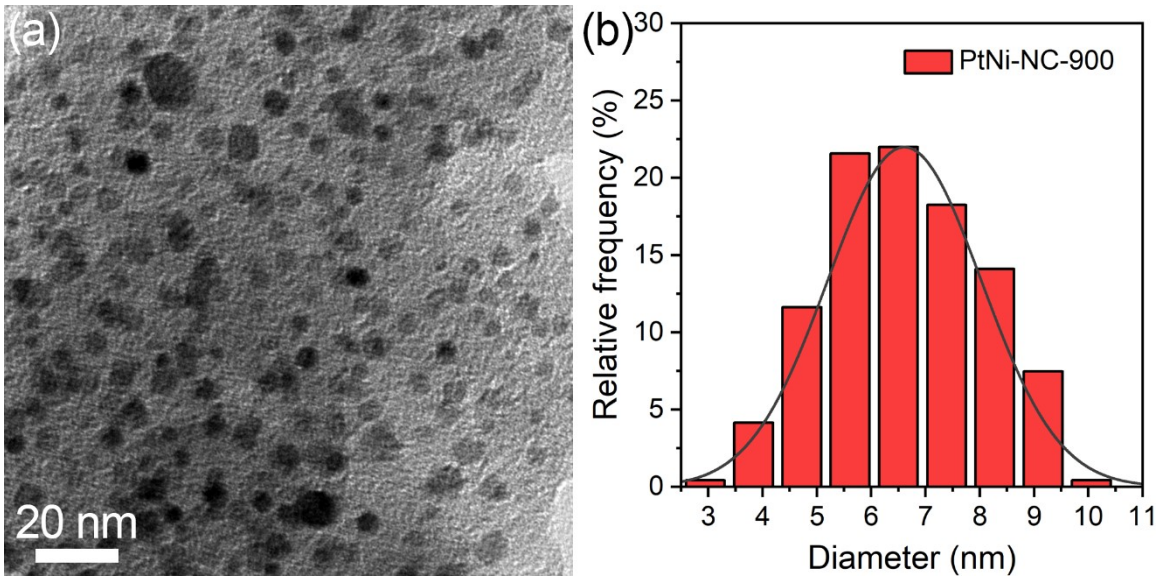

Fig. S2 (a) TEM image and (b) corresponding PtNi nanoparticle size distribution of PtNi-NC-900.

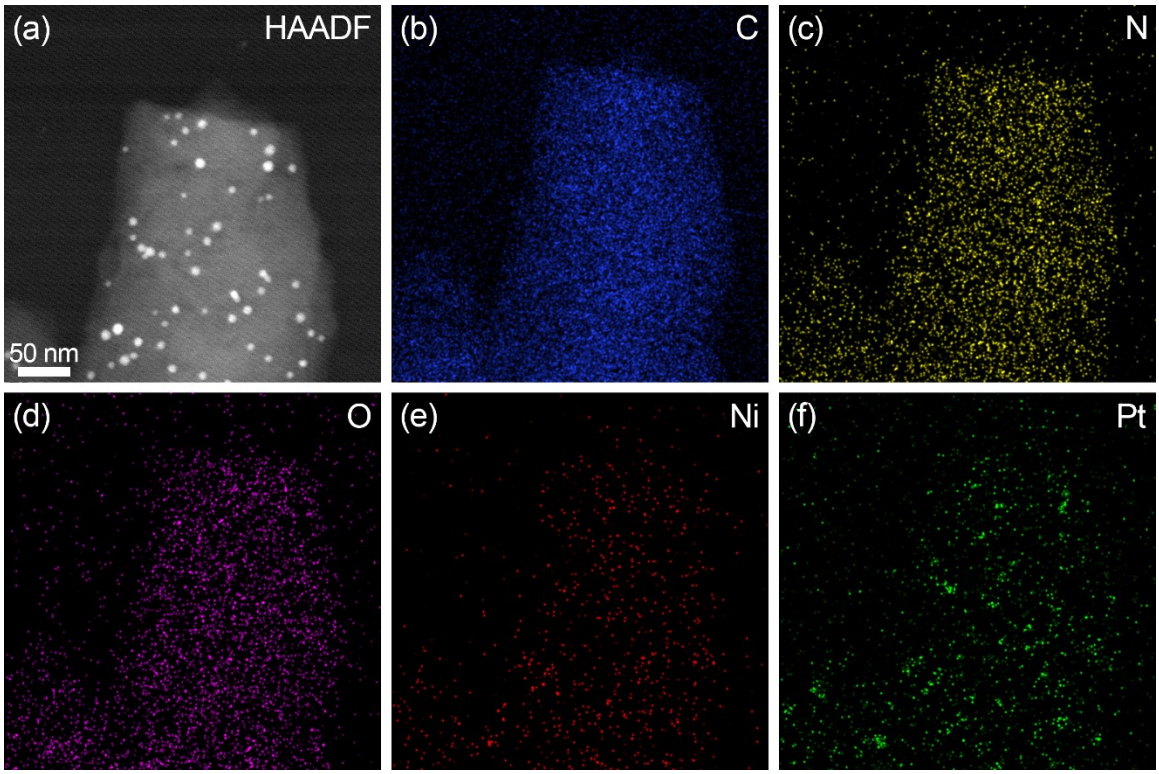

Fig. S3 (a) HAADF image of PtNi-NC-900 and corresponding element mappings images for (b) C, (c) N, (d) O, (e) Ni, and (f) Pt.

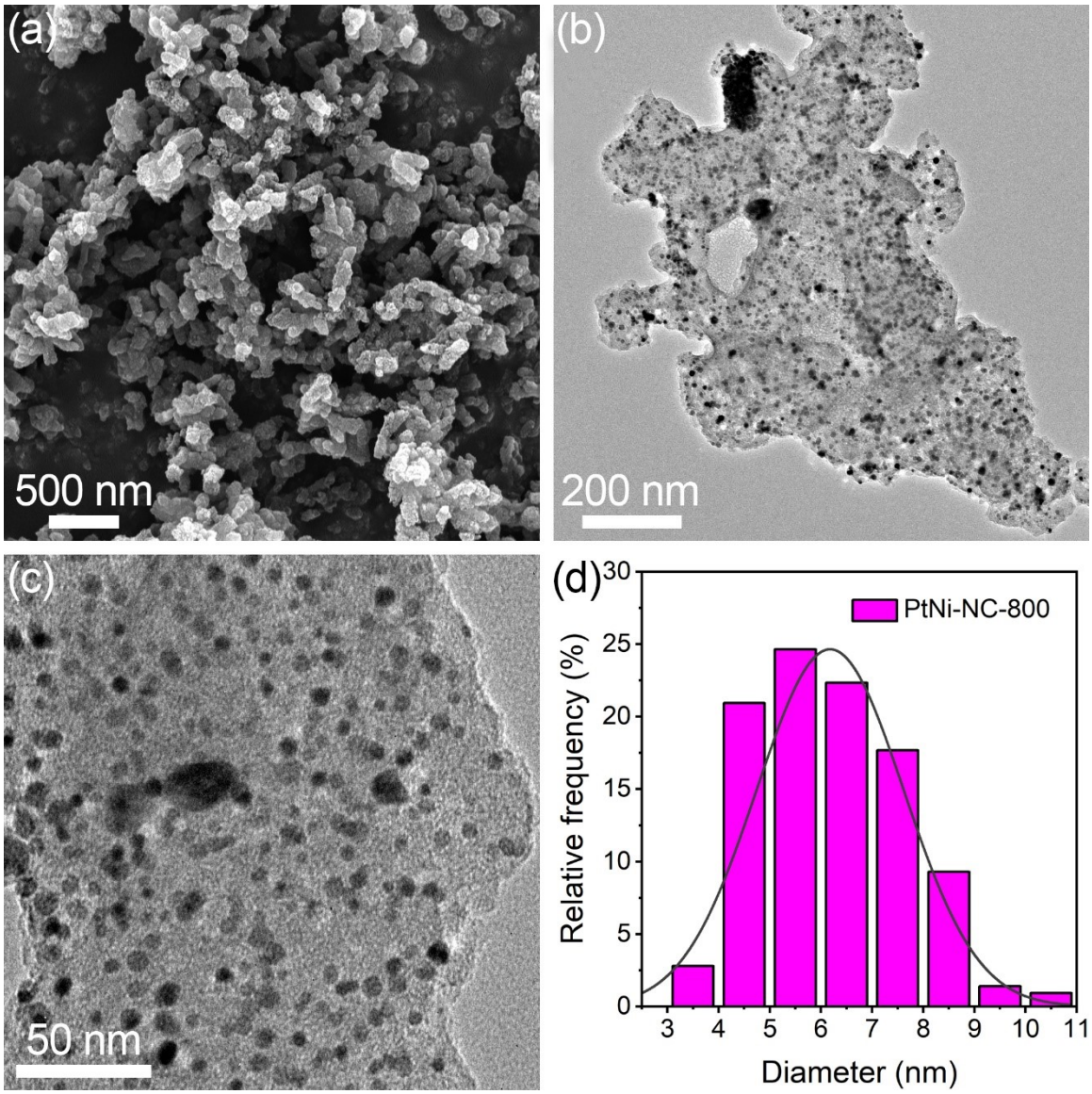

Fig. S4 (a) SEM image, (b,c) TEM images, and (d) PtNi nanoparticle size distribution of PtNi-NC-800.

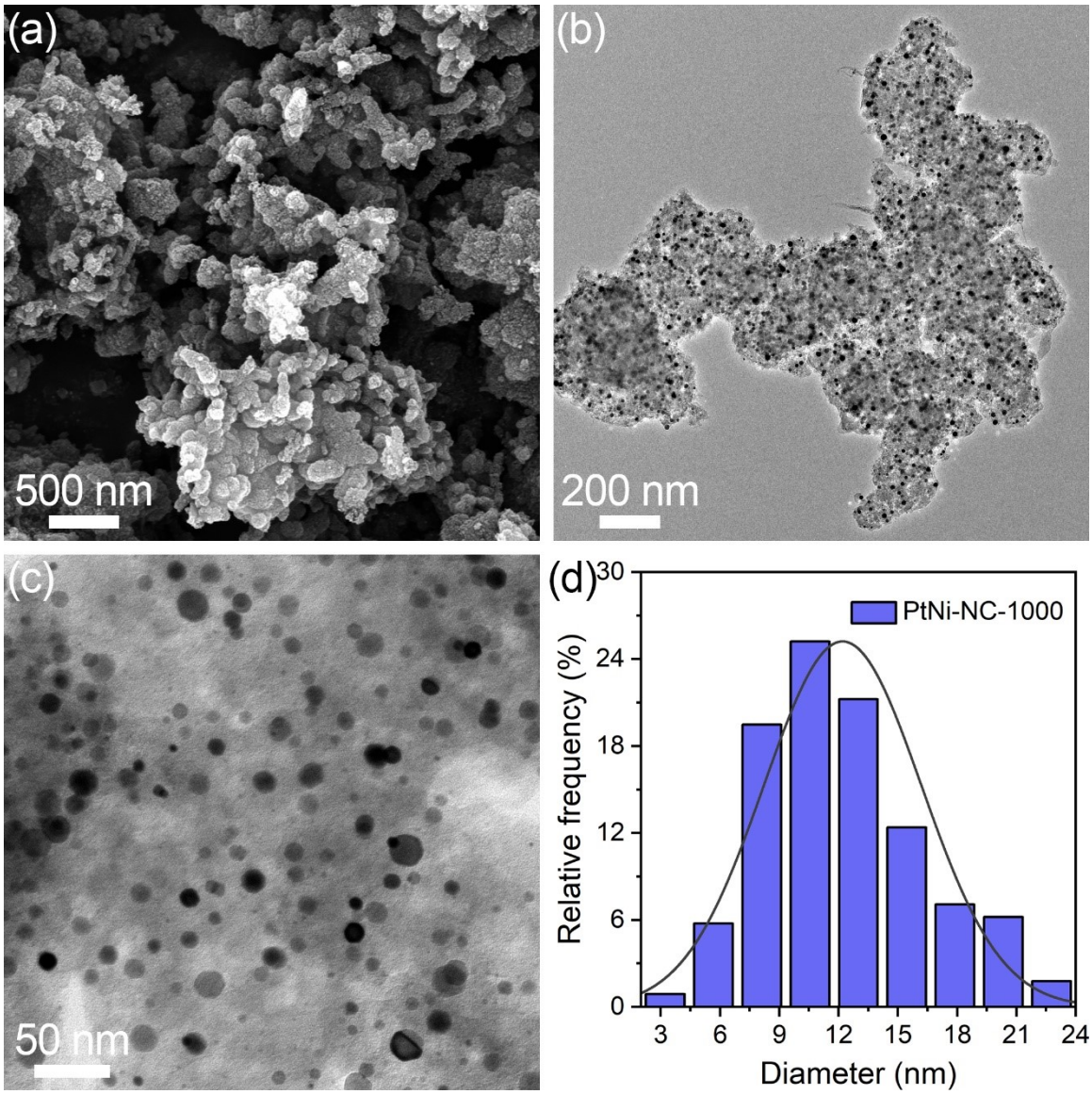

Fig. S5 (a) SEM image, (b,c) TEM images, and (d) PtNi nanoparticle size distribution of PtNi-NC-1000.

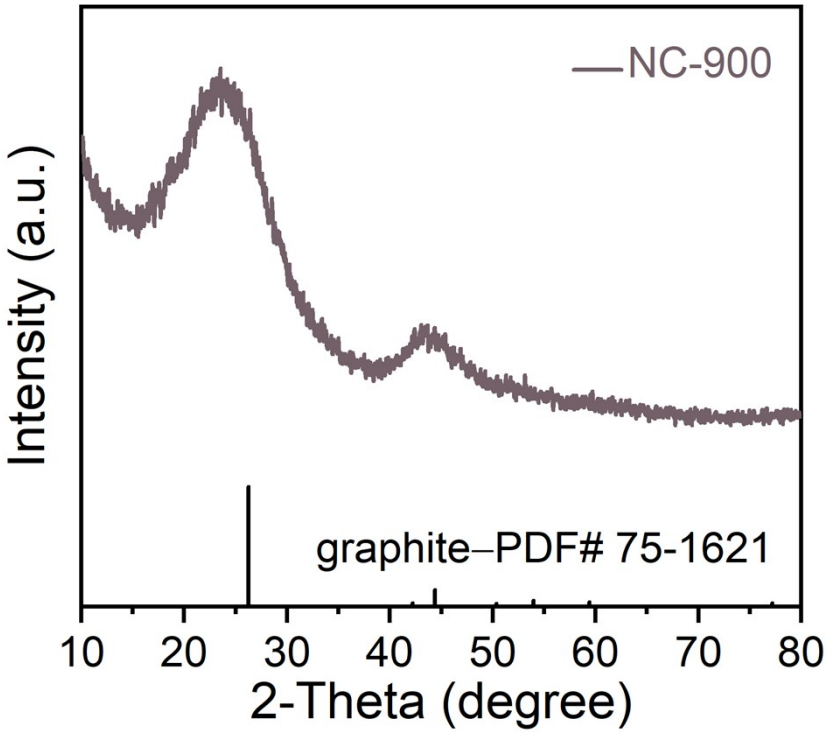

Fig. S6. XRD pattern of NC-900.

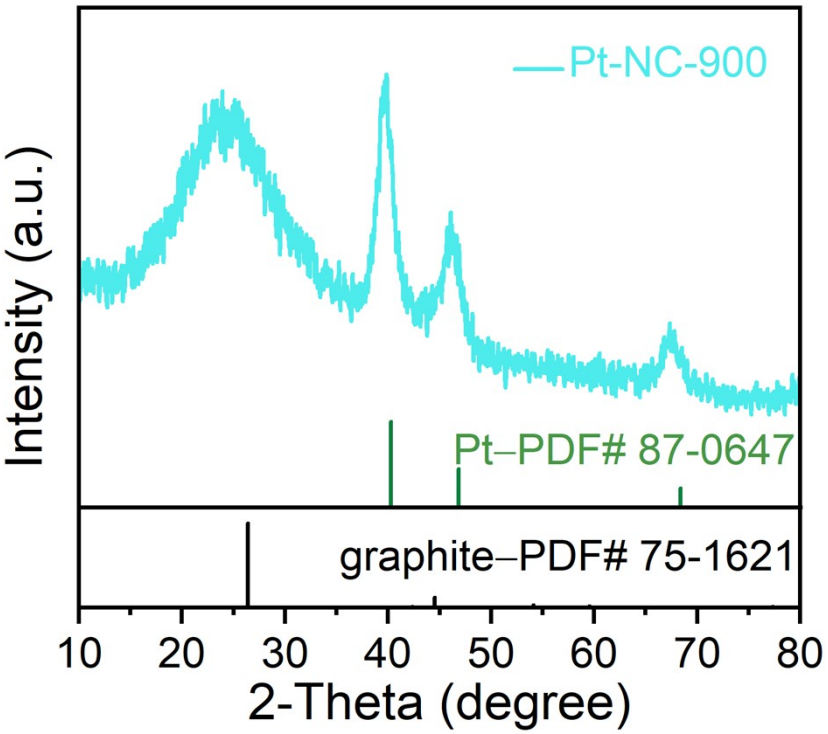

Fig. S7 XRD pattern of Pt-NC-900.

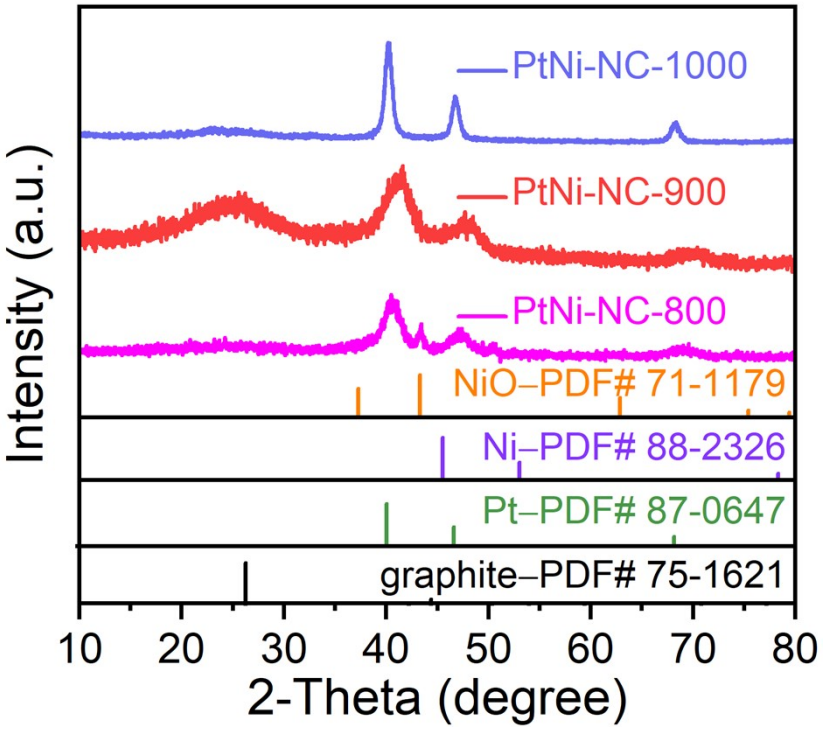

Fig. S8 XRD patterns of PtNi-NC-800, PtNi-NC-900, and PtNi-NC-1000.

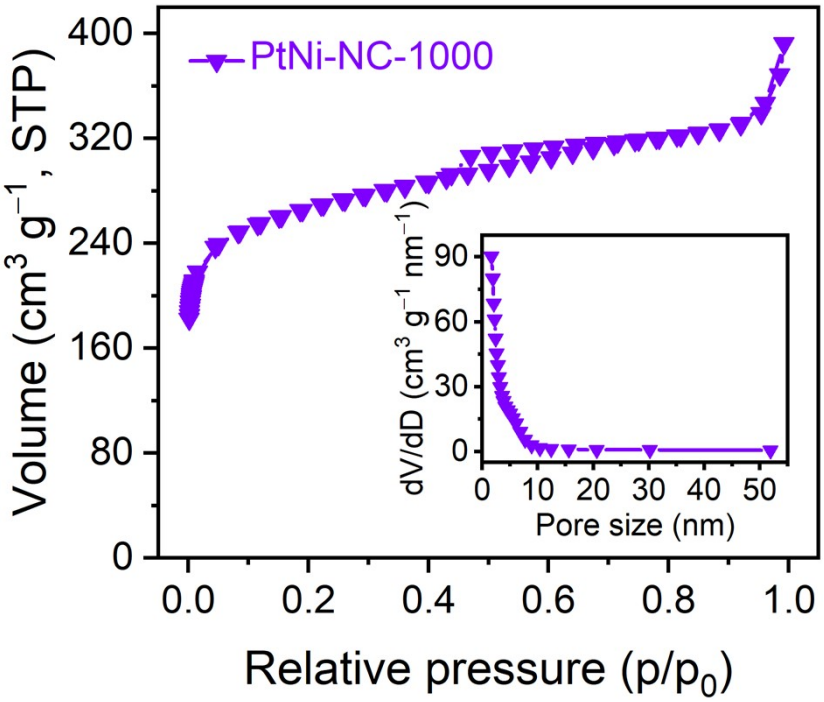

Fig. S9 N_2 adsorption-desorption isotherm and corresponding pore size distribution of PtNi-NC-1000.

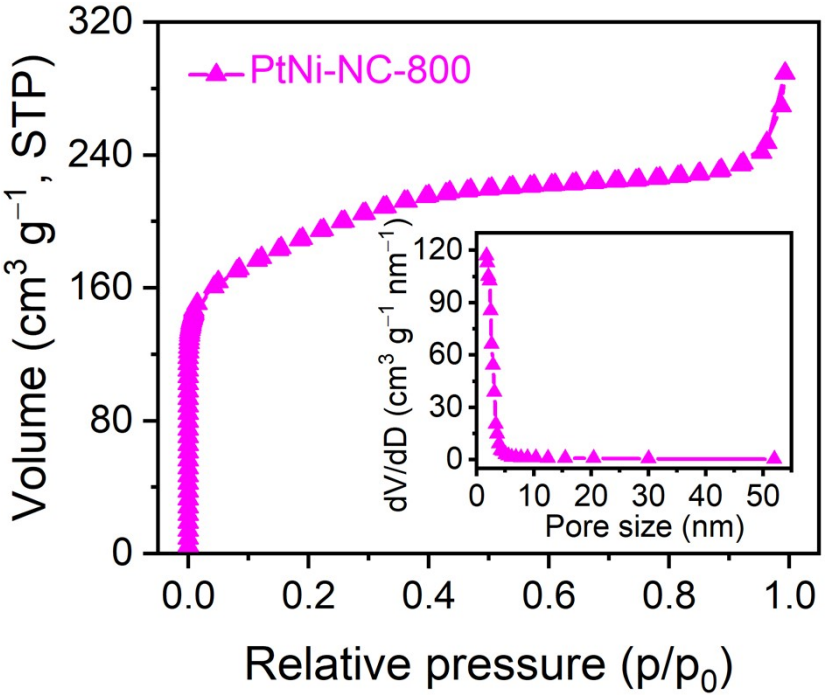

Fig. S10 N_2 adsorption-desorption isotherm and corresponding pore size distribution of PtNi-NC-800.

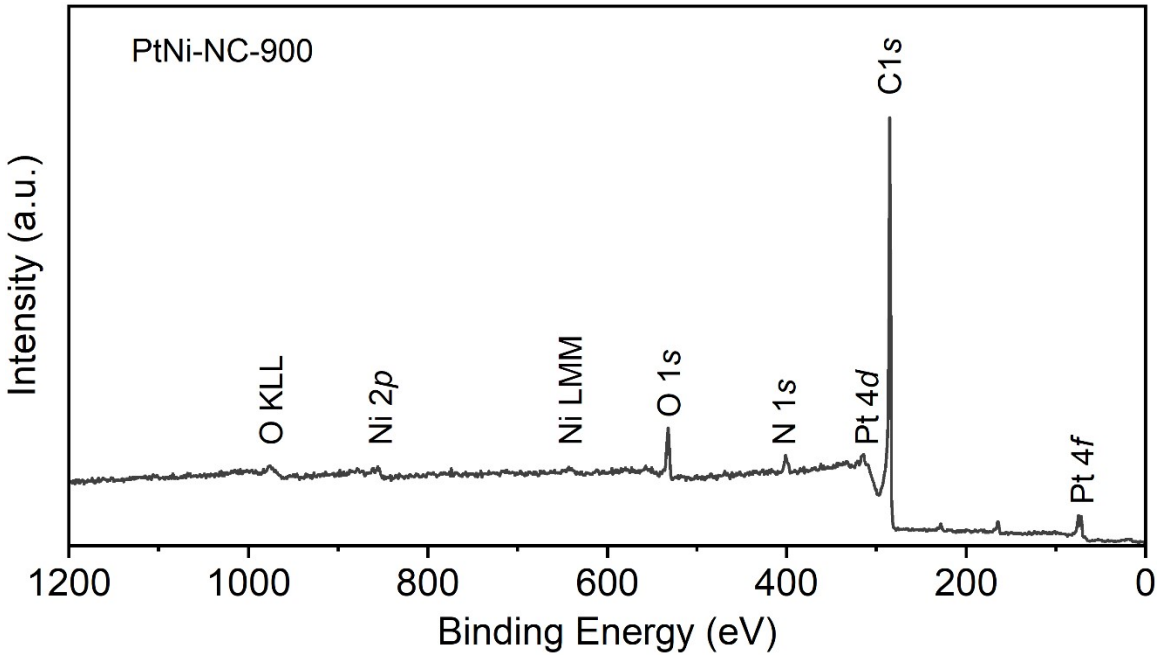

Fig. S11 Survey XPS spectrum of PtNi-NC-900.

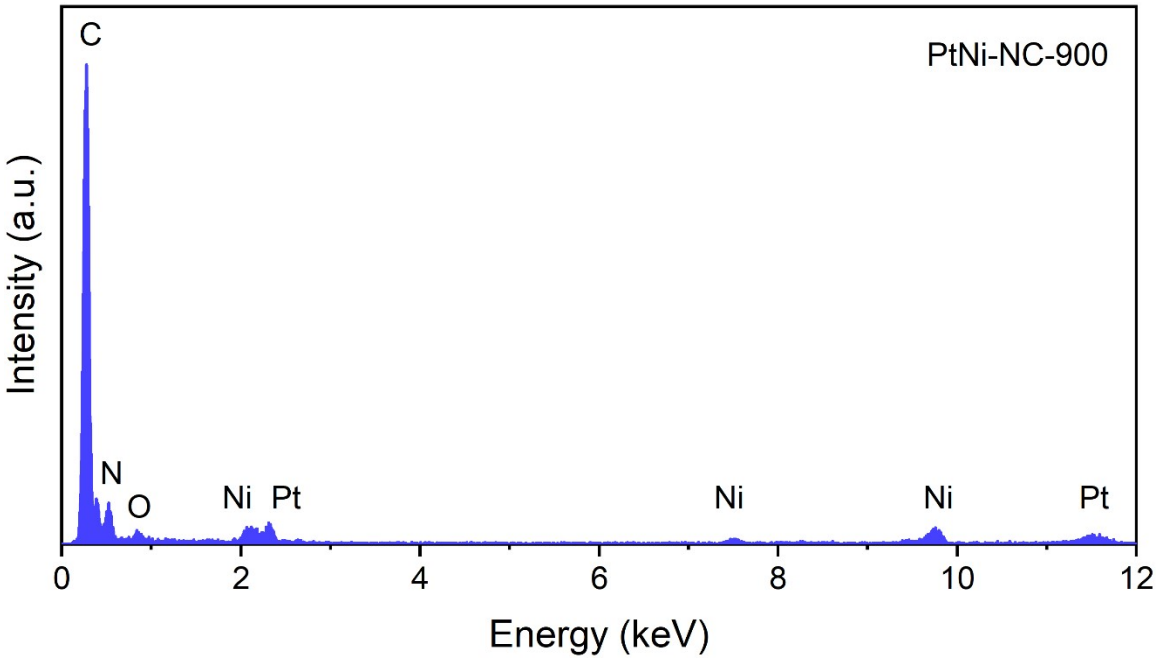

Fig. S12 EDX spectrum of PtNi-NC-900.

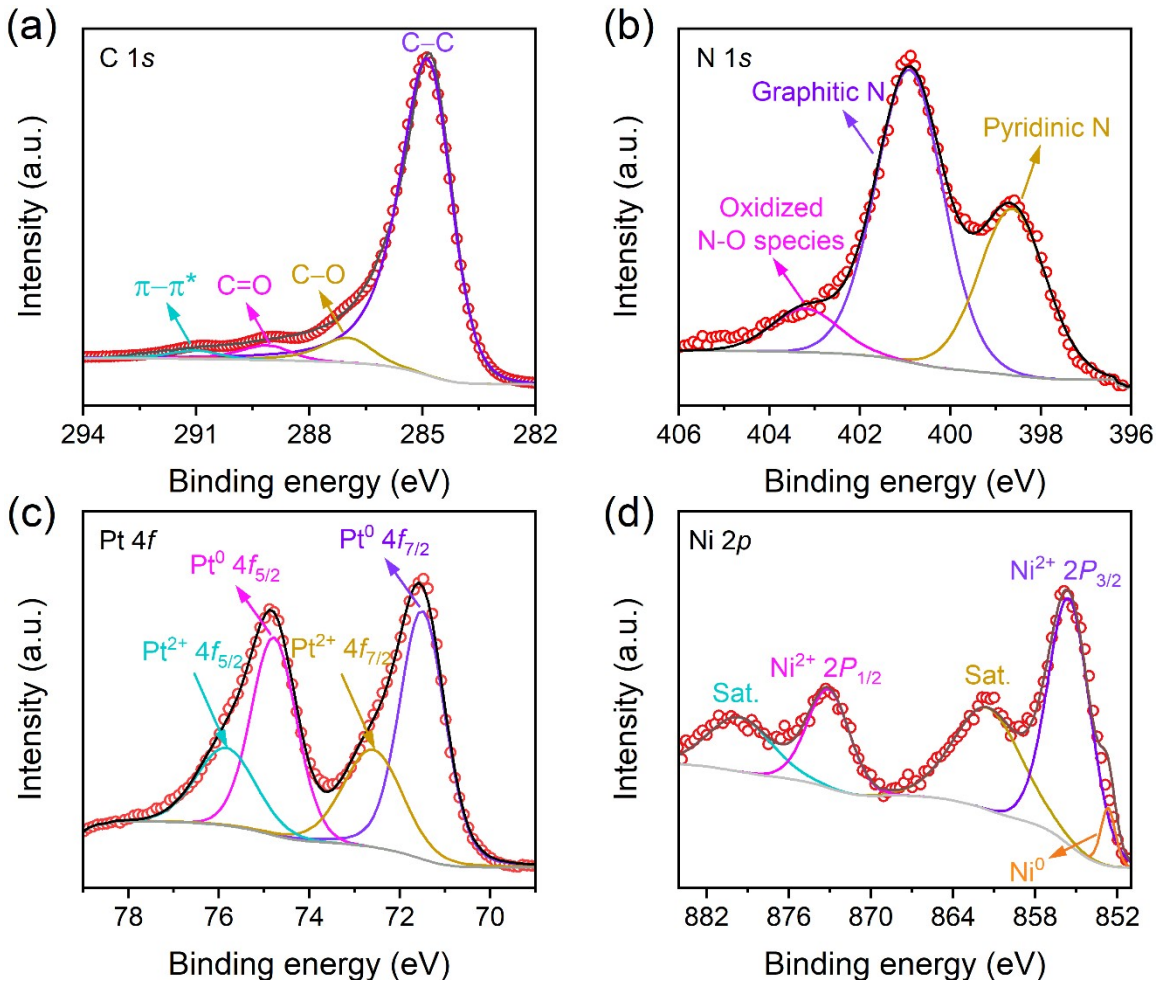

Fig. S13 (a) C 1s, (b) N 1s, (c) Pt 4f, and (d) Ni 2p XPS spectra of PtNi-NC-800.

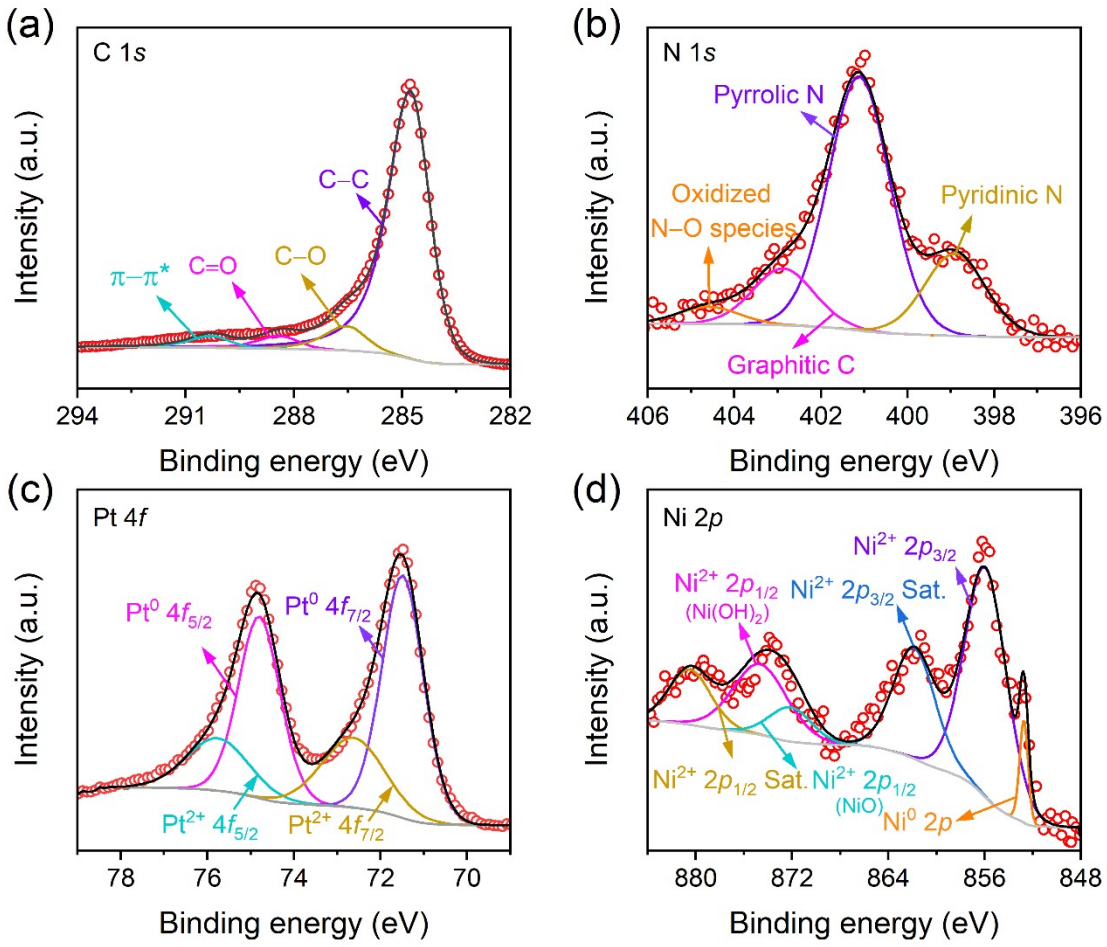

Fig. S14 (a) C 1s, (b) N 1s, (c) Pt 4f, and (d) Ni 2p XPS spectra of PtNi-NC-1000.

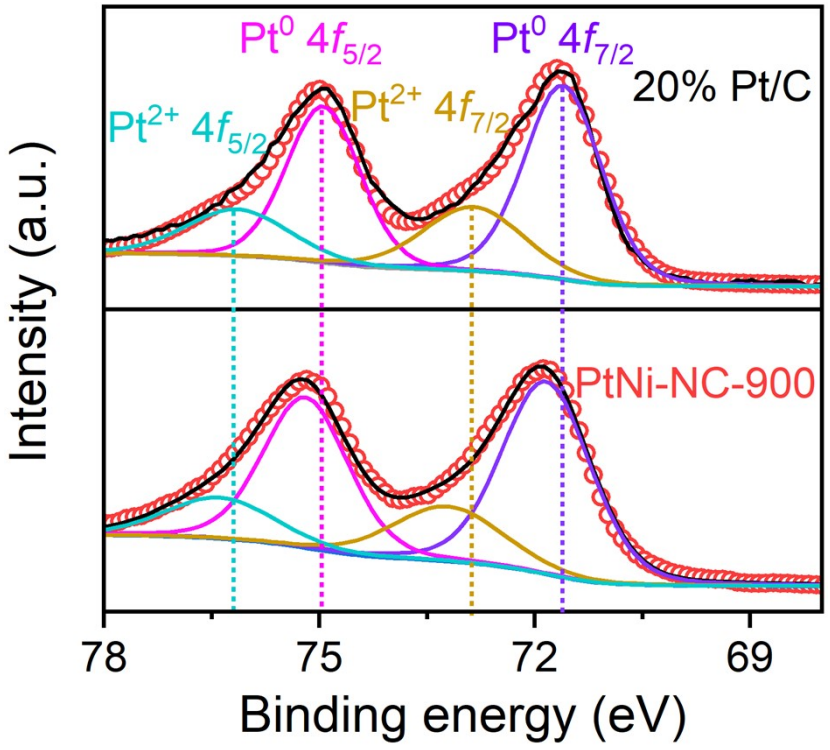

Fig. S15 Pt 4f XPS spectra of 20% Pt/C and PtNi-NC-900.

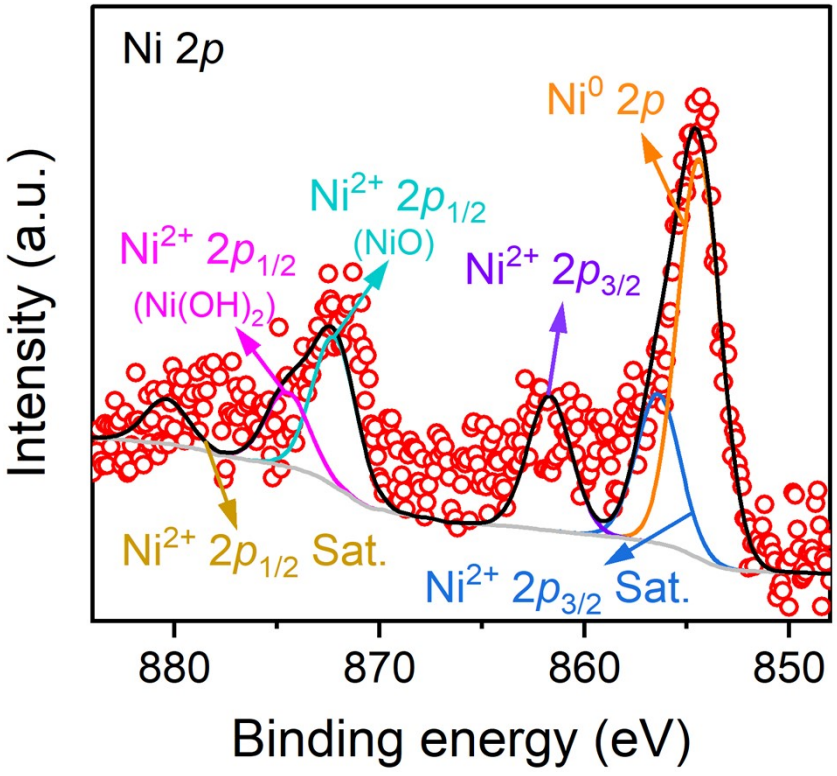

Fig. S16 Ni 2p XPS spectrum of Ni-NC-900.

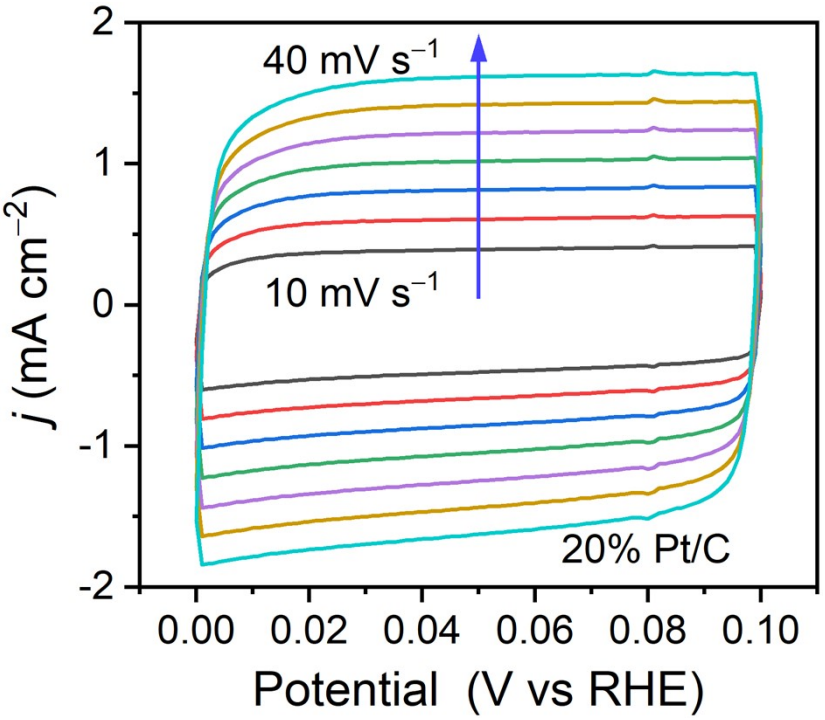

Fig. S17 CV curves of 20% Pt/C at various scan rates from 10 to 40 mV s^{-1} in 0−0.1 V vs RHE.

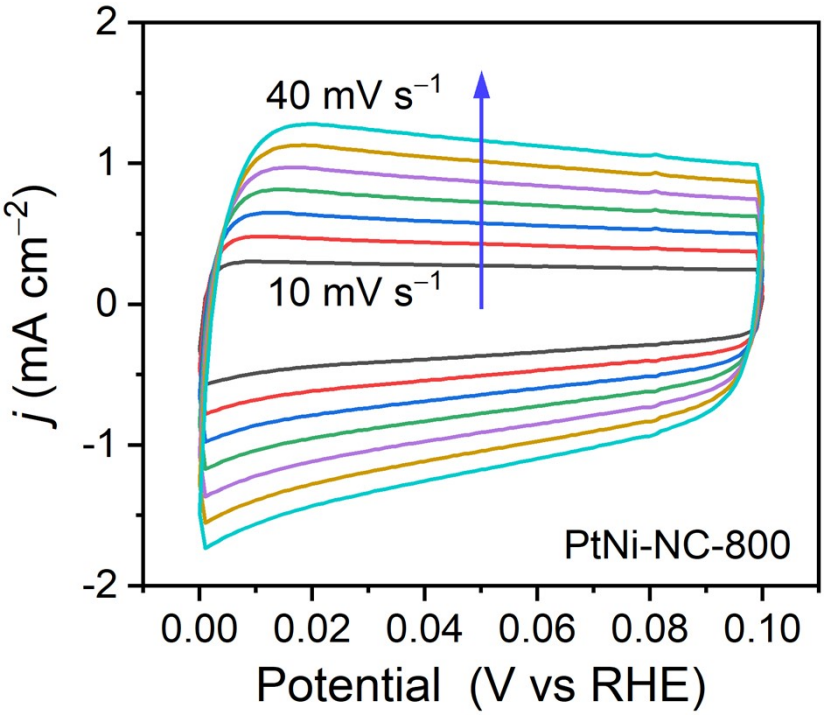

Fig. S18 CV curves of PtNi-NC-800 at various scan rates from 10 to 40 mV s^{-1} in 0−0.1 V vs RHE.

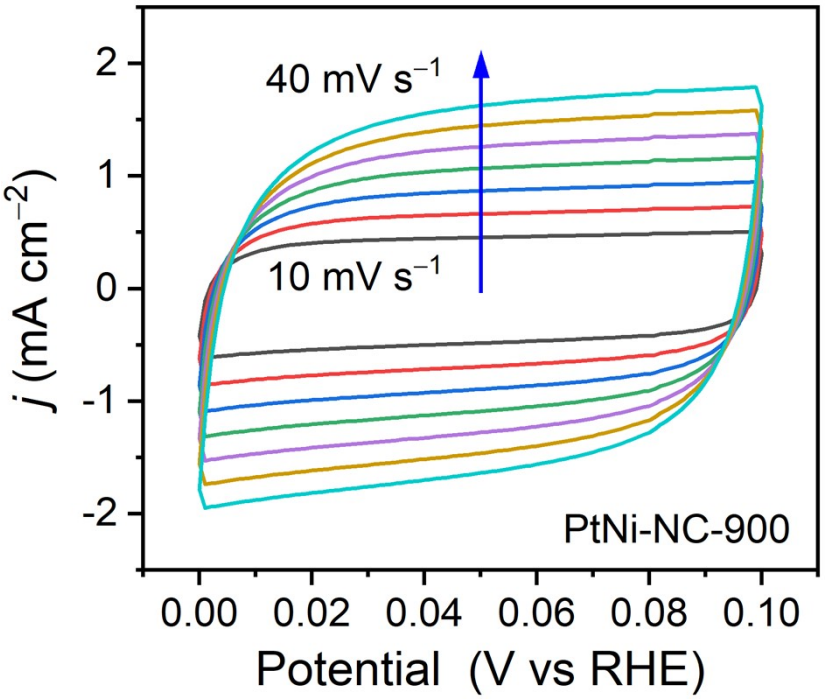

Fig. S19 CV curves of PtNi-NC-900 at various scan rates from 10 to 40 mV s^{-1} in 0–0.1 V vs RHE.

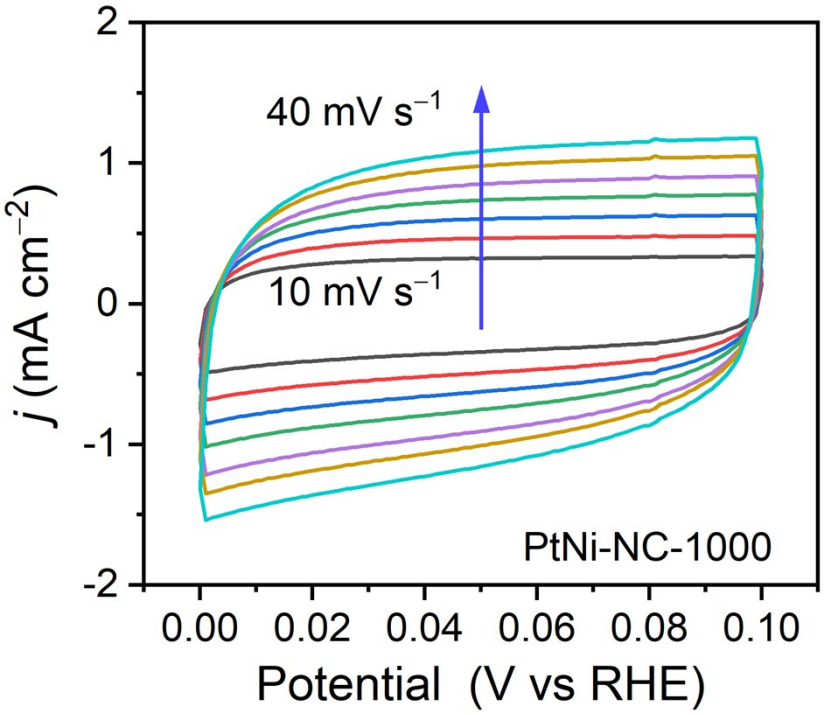

Fig. S20 CV curves of PtNi-NC-1000 at various scan rates from 10 to 40 mV s^{-1} in 0–0.1 V vs RHE.

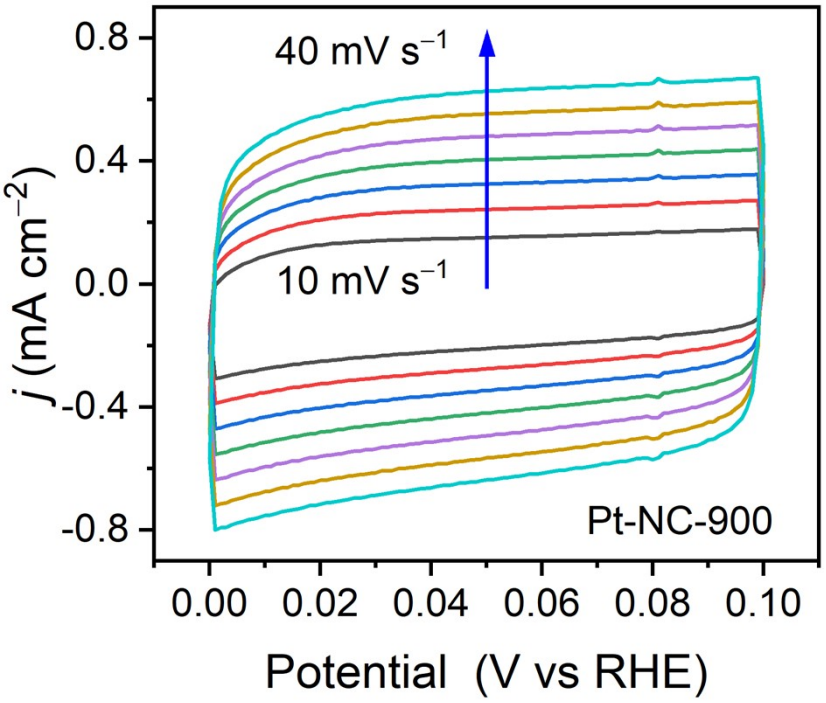

Fig. S21 CV curves of Pt-NC-900 at various scan rates from 10 to 40 mV s^{-1} in 0−0.1 V vs RHE.

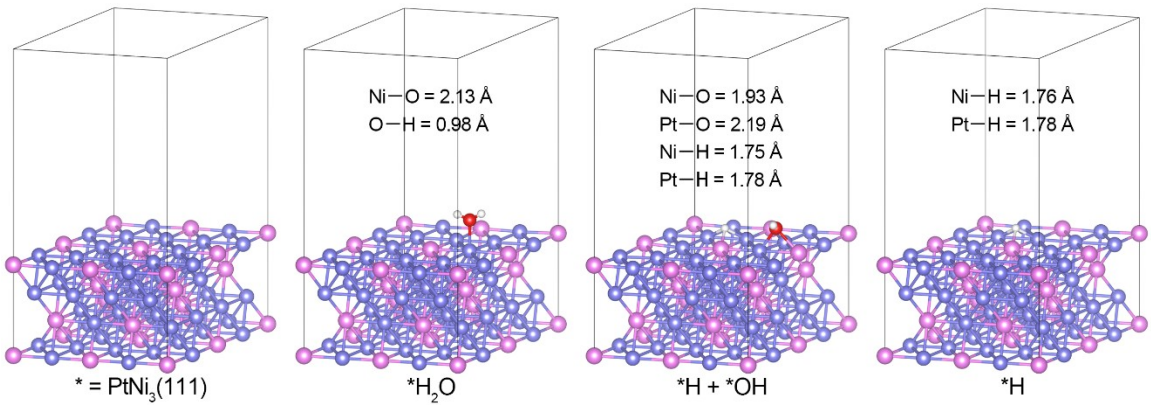

Fig. S22 Atomic configurations of optimized $PtNi_3(111)$ slab and its corresponding alkaline HER intermediates, where magenta, purple, red, and white spheres represent Pt, Ni, O, and H atoms, respectively.

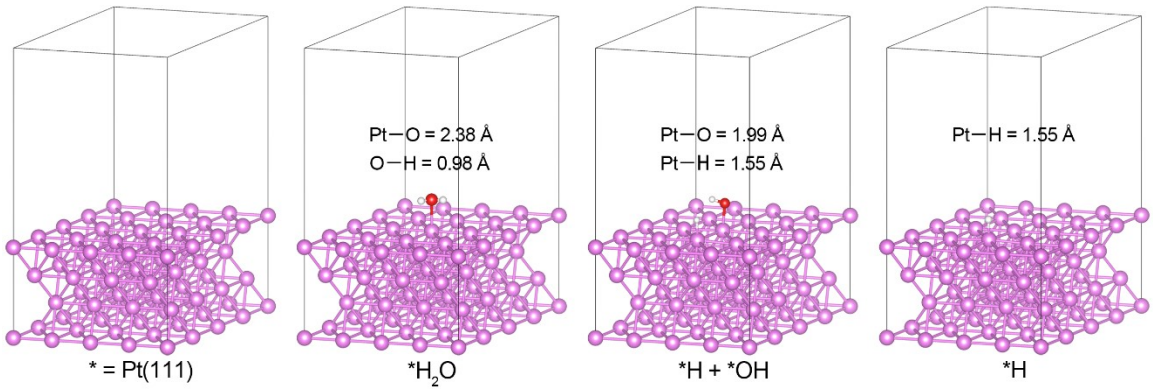

Fig. S23 Atomic configurations of optimized Pt(111) slab and its corresponding alkaline HER intermediates, where magenta, red, and white spheres represent Pt, O, and H atoms, respectively.

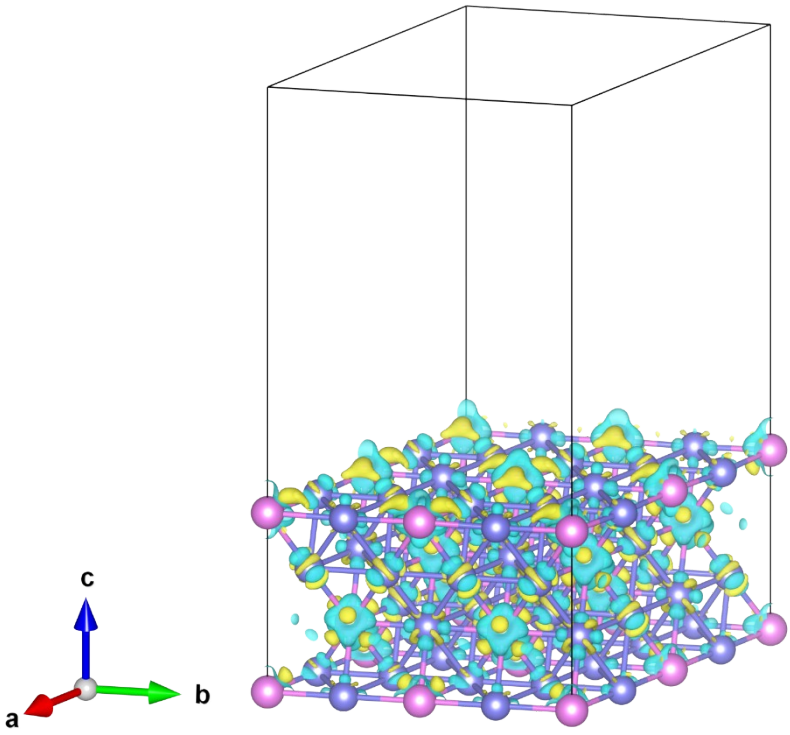

Fig. S24 Difference charge density of pristine $PtNi_3$(111) surface (where cyan areas show an electron density decrease and yellow areas an electron density increase).

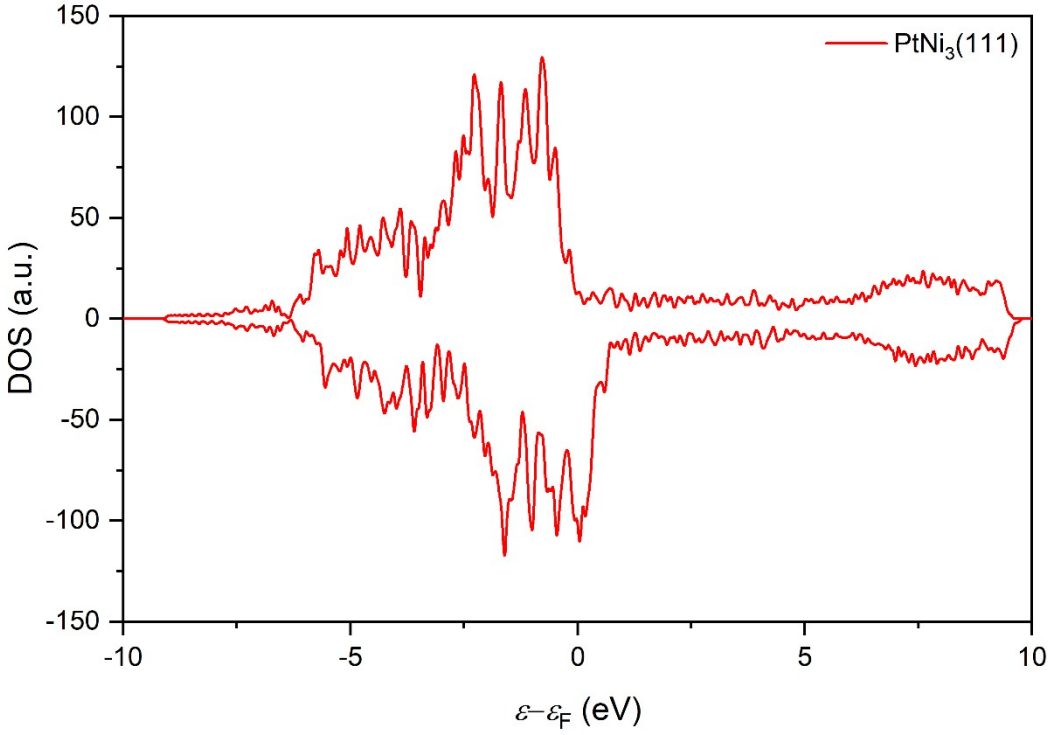

Fig. S25 Total DOS of $PtNi_3(111)$.

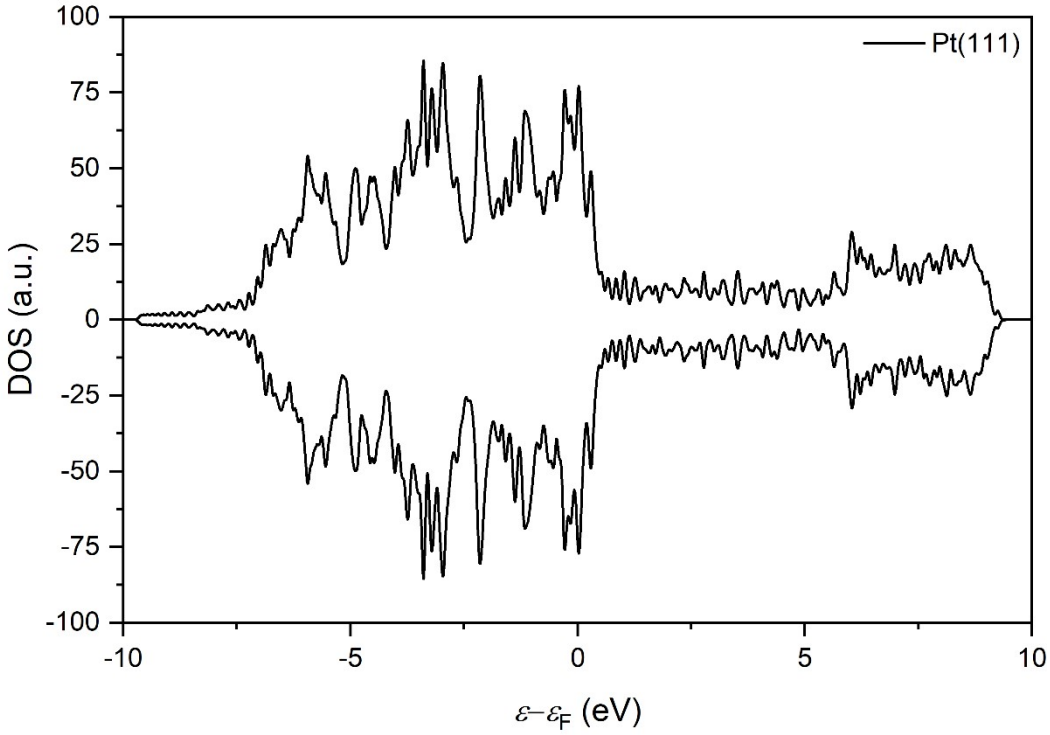

Fig. S26 Total DOS of Pt(111).

Table S1 Comparison of the positions of deconvoluted Ni 2p peaks for PtNi-NC-900 and Ni-NC-900

Sample	Ni^0	$Ni^{2+}2P_{3/2}$	$Ni^{2+}2P_{3/2}$ Sat.	$Ni^{2+}2P_{1/2}$ ($Ni(OH)_2$)	$Ni^{2+}2P_{1/2}$ (NiO)	$Ni^{2+}2P_{1/2}$ Sat.
PtNi-NC-900	854.2 eV	856.3 eV	861.5 eV	874.3 eV	872.1 eV	880.2 eV
Ni-NC-900	854.4 eV	856.4 eV	861.7 eV	874.5 eV	872.2 eV	880.4 eV

Table S2 Comparison of the HER activities of PtNi-NC-900 and other recently reported Pt and Ni based electrocatalysts in 1.0 M KOH

Catalyst	Mass activity	Current Density	Overpotential (mV)	Tafel Slope (mV dec^{-1})	Ref.
PtNi-NC-900	3.78 A mg_{Pt}^{-1} (@50 mV)	31.7 (–0.07 V)	37.4 mV (@10 Am cm^{-2})	43.2	This work
PtNi-O/C	7.23 A mg_{Pt}^{-1} (@70 mV)	14.8 (–0.07 V)	39.8 mV (@10 Am cm^{-2})	78.8	10
PtNWs/SL -$Ni(OH)_2$	0.679 A mg_{Pt}^{-1} (@70 mV)	10.9 (–0.07 V)	70 mV (@10 Am cm^{-2})	–	11
Pt_2Ni_3-P NWs	–	–	44 mV (@10 Am cm^{-2})	66	12
Pt_2Ni_3-NWs	–	–	51 mV (@10 Am cm^{-2})	85	12
Pt_3Ni_3NWs/C-air	–	39.7 (–0.07 V)	40 mV (@10 Am cm^{-2})	–	13
D-PtNi/C	1.03 A mg_{Pt}^{-1} (@70 mV)	–	39.7 mV (@10 Am cm^{-2})	55	14
20 wt% Pt/$Ni(HCO_3)_2$	1.77 A mg_{Pt}^{-1} (@100 mV)	–	44 (@10 Am cm^{-2})	45	15
38 wt% Pt NWs/SL-$Ni(OH)_2$	0.68 A mg_{Pt}^{-1} (@70 mV)	2.48 (–0.07 V)	85.5 (@4 Am cm^{-2})	–	16

References

1 G. Kresse and J. Hafner, *Phys. Rev. B*, 1993, **47**, 558−561.

2 G. Kresse and J. Hafner, *Phys. Rev. B*, 1994, **49**, 14251−14269.

3 X. Liu, Y. Jiao, Y. Zheng, K. Davey and S.-Z. Qiao, *J. Mater. Chem. A*, 2019, **7**, 3648–3654.

4 Y.-L. Wu, X. Li, Y.-S. Wei, Z. Fu, W. Wei, X.-T. Wu, Q.-L. Zhu and Q. Xu, *Adv. Mater.*, 2021, **33**, 2006965.

5 P. E. Blöchl, *Phys. Rev. B*, 1994, **50**, 17953−17979.

6 G. Kresse and D. Joubert, *Phys. Rev. B*, 1999, **59**, 1758−1775.

7 J. P. Perdew, K. Burke and M. Ernzerhof, *Phys. Rev. Lett.*, 1996, **77**, 3865−3868.

8 S. Grimme, *J. Comput. Chem.*, 2006, **27**, 1787−1799.

9 J. K. Nørskov, J. Rossmeisl, A. Logadottir, L. Lindqvist, J. R. Kitchin, T. Bligaard and H. Jónsson, *J. Phys. Chem. B*, 2004, **108**, 17886−17892.

10 Z. Zhao, H. Liu, W. Gao, W. Xue, Z. Liu, J. Huang, X. Pan and Y. Huang, *J. Am. Chem. Soc.*, 2018, **140**, 9046-9050.

11 Z. Cao, Q. Chen, J. Zhang, H. Li, Y. Jiang, S. Shen, G. Fu, B. A. Lu, Z. Xie and L. Zheng, *Nat. commun.*, 2017, **8**, 15131.

12 P. Wang, Q. Shao, J. Guo, L. Bu and X. Huang, *Chem. Mater.*, 2020, **32**, 3144-3149.

13 P. Wang, K. Jiang, G. Wang, J. Yao and X. Huang, *Angew. Chem. Int. Ed.*, 2016, **55**, 12859-12863.

14 H. Chen, G. Wang, T. Gao, Y. Chen, H. Liao, X. Guo, H. Li, R. Liu, M. Dou, S. Nan and Q. He, *J. Phys. Chem. C*, 2020, **124**, 5036-5045.

15 M. Lao, K. Rui, G. Zhao, P. Cui, X. Zheng, S. X. Dou and W. Sun, *Angew. Chem. Int. Ed.*, 2019, **58**, 5432-5437.

16 H. Yin, S. Zhao, K. Zhao, A. Muqsit, H. Tang, L. Chang, H. Zhao, Y. Gao and Z. Tang, *Nat. Commun.*, 2015, **6**, 6430.